Novel lymph node segmentation and proliferation index measurement for skin melanoma biopsy images

Salah Alheejawi [a], Hongming Xu [a], Richard Berendt [b], Naresh Jha [b], Mrinal Mandal [a,*]

[a] University of Alberta, Edmonton, AB, T6G 2V4, Canada
[b] Department of Oncology, Cross Cancer Institute, University of Alberta, Edmonton, AB, T6G 1Z2, Canada

ABSTRACT

The lymphatic system is the immune system of the human body, and includes networks of vessels spread over the body, lymph nodes, and lymph fluid. The lymph nodes are considered as purification units that collect the lymph fluid from the lymph vessels. Since the lymph nodes collect the cancer cells that escape from a malignant tumor and try to spread to the rest of the body, the lymph node analysis is important for staging many types skin and breast cancers. In this paper, we propose a Computer Aided Diagnosis (CAD) method that segments the lymph nodes and melanoma regions in a biopsy image and measure the proliferation index. The proposed method contains two stages. First, an automated technique is used to segment the lymph nodes in a biopsy image based on histogram and high frequency features. In the second stage, the proliferation index for the melanoma regions is calculated by comparing the number of active and passive nuclei. Experimental results on 76 different lymph node images show that the proposed segmentation technique can robustly segment the lymph nodes with more than 90% accuracy. The proposed proliferation index calculation has low complexity and has an average error rate of less than 1.5%.

© 2019 Elsevier Ltd. All rights reserved.

1. Introduction

Melanoma is a dangerous type of skin cancer, spread around the world, though it is less common compared to other cancer types such as Lung, Prostate, Breast cancer (American Cancer Society, 2018; International Agency for Research on Cancer, 2014). Melanoma is caused by the aggressive growth of melanocytes typically found around the epidermis-dermis junction. Due to excessive exposure to ultraviolet radiation, the nucleus DNA of melanocytes may be damaged causing abnormal growth. Melanoma shows aggressive and unpredictable behaviour which can spread to any part of the body. As per a recent statistic, about 96,480 people would be diagnosed with invasive melanoma, and about 7230 would die from it in the United states alone in 2019 (Siegel et al., 2019). Once melanoma is diagnosed by analysing skin epidermis/dermis layer, the doctors typically do a lymph node biopsy to determine if melanoma has invaded the lymph node system (Xu and Mandal, 2015; Xu et al., 2017). The melanoma passes to lymph nodes through the lymph vessels, after invading the epidermis/dermis layers. It is important to diagnose and grade the melanoma in Sen-

tinel Lymph Nodes (SLN), because it is the stage where melanoma can spread to different organs in the body through the lymph vessels (Balch et al., 2010). The diagnosis is done by removing an SLN biopsy (SLNB) (Giuliano et al., 1994; Nawaz et al., 2016). The SLNB is sliced into very thin layers that are placed on a glass slide with histology stains for examination under a microscope by pathologists (see Fig.1). Traditionally, the pathologists examine an SLNB slide under a microscope and a diagnosis is made based on their personal experience and knowledge, which are sometimes subjective and is prone to intra- and inter-observer variability (Ismail et al., 1989; Petushi et al., 2006). With technological advances in digital imaging and computer hardware, the biopsy image can be digitized and analyzed using automated image analysis techniques. The automated computer-aided image analysis can provide fast diagnosis, and reliable and reproducible objective results (Wang et al., 2009). However, computer aided analysis of biopsy images faces many challenges such as the blurry appearance due the slicing process of the tissue, the low contrast for some parts of the tissue and sectioning artifacts (e.g., missing and folding in some parts of the tissue) (Wu et al., 2019; Kothari et al., 2013).

To the author's knowledge, no technique has appeared in the literature for automated lymph node segmentation of biopsy image. However, a few techniques have been proposed in the literature, for SLN segmentation in the Computed Tomography (CT) and *ultra-*

* Corresponding author.
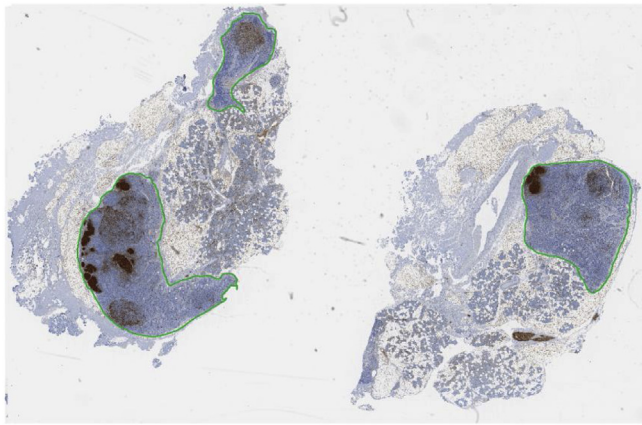 *E-mail address:* mmandal@ualberta.ca (M. Mandal).

Fig. 1. A sentinel lymph node (SLN) biopsy with S-100 staining. The three lymph nodes are shown with green contour.

sound for breast cancer. These images have different characteristic compared to lymph node biopsy for detecting the skin cancer. Steger et al. (2011) proposed a lymph node segmentation technique in CT slices using gradient, intensity and shape information. Zhang et al. (2016) proposed a lymph node segmentation technique in ultrasound image by using a convolutional neural network.

The proliferation index (PI) is an important diagnostic and prognostic factor for cancer diagnosis. The proliferation index is measured by estimating the ratio of the numbers of active nuclei and all nuclei (Hanahan and Weinberg, 2011). It is known that Ki-67 protein is present during all active phases of a cell cycle (G_1, S, G_2, and mitosis), but is absent in resting passive phase (G_0) (Bruno and Darzynkiewicz, 1992). A special Ki-67 stain is typically used to stain this protein and identify the active nuclei (Bánkfalvi, 2000). In a Ki-67 stained image, the nuclei appear with two colors: the active nuclei appear dark brown and passive nuclei appear blue.

Mungle et al. (Mungle and Tewary, 2017) proposed a technique to measure the PI in a Ki-67 stained breast biopsy image. In this technique, a pathologist manually identifies a few windows of tumor regions with high concentration of active nuclei. A Fuzzy C-means (FCM) based thresholding technique is used to separate the nuclei from the background. K-means clustering technique is then used to classify the active and passive nuclei pixels. By comparing the areas of active and passive nuclei, the PI value is calculated. This technique requires input from a pathologist to identify the dense active nuclei regions. The FCM-based thresholding and K-means clustering, being iterative, have high computational complexity. In addition, the unsupervised K-means clustering technique may not perform well to classify the active and passive nuclei.

In this paper, we propose a fully automated technique to segment the lymph node tissues and measure the PI in biopsy images. The biopsy images may be stained with different histology stains such as Hematoxylin and Eosin (H&E), MART-1, S-100, CD-45 and Ki-67 stains (Alturkistani et al., 2016). For lymph node segmentation, the proposed technique segments lymph nodes using histogram and high-frequency local features. For PI calculation, it is assumed that a lymph node biopsy is stained with both MART-1 and Ki-67. The MART-1 stain is used to identify the melanoma regions by detecting a special protein called MART-1 that exists on the surface of melanocytes and the Ki-67 stain is used to detect the proliferative activity of the lymph node nuclei. In the proposed technique, the melanoma regions obtained from MART-1 images are mapped onto the corresponding Ki-67 image to automatically identify the melanoma regions in the Ki-67 image. Active and passive nuclei in the melanoma regions are then detected using Otsu thresholding and SVM classification. By comparing the number of active and passive nuclei, the PI value is calculated.

The organization of the paper is as follows. Section 2 describes the dataset; Section 3 describes the lymph node segmentation technique in detail, followed by the PI calculation in Section 4. The conclusion is presented in Section 5.

2. Data description

In this study, all lymph node histopathological images are collected from the Cross Cancer Institute, University of Alberta in accordance with the protocol for the examination of specimens with skin melanoma. The histological sections of lymph node tissues are about 4 μm thick and are stained with different stains such as H&E, MART-1, S100, CD-45 and Ki-67 stain. The digital images were captured under 40X magnification on Aperio Scanscope CS scanning system (0.25 μm/pixel resolution) with default calibration and illuminance settings (based on Aperio service notes). In this study, 39 WSI from nine patients are used to evaluate the proposed technique. Each of the nine patients has one MART-1, one H&E, one Ki-67 (total 27) stained WSI. Five patients have one CD-45 WSI each, and seven patients have one S100 WSI each. In other words, 39 WSIs include 9 H&E, 9 MART-1, 9 KI-67, 5 CD-45, and 7 S-100 images. Each WSIs in the dataset contain 2–4 lymph nodes. In this data set, there are 17 unique lymph nodes, and after staining with different stains there are 69 lymph nodes. The ground truth (segmented LN) images were obtained by manual segmentation by doctors. Fig. 1 shows a WSI stained with S-100 and the lymph nodes are shown using a green contour.

3. Lymph node segmentation

The schematic of lymph node and melanoma segmentation is shown in Fig.2, which consists of three modules: Coarse Segmentation, Features Extraction, and Fine Segmentation. The details of each module are presented in the following.

3.1. Coarse segmentation

Most SLNB images consist of four regions (see Fig. 1): melanoma metastasis (dark brown pixels), lymph node tissues (pixels within green line), other tissues (e.g. remains of dermis, fat, parts of other lymph tissues, etc) and white background (which is not part of the actual biopsy slice). In this module, a coarse segmentation is performed using the histogram of the gray intensity image. This module calculates the required thresholds to classify the image into four classes: *Class 1* (Melanoma), *Class 2* (Lymph node tissue), *Class 3* (Other tissue) and *Class 4* (Background). The thresholds are determined based on the local minimum values of the smoothed image histogram (see Fig.3). The classified image pixels $I(x, y)$, $1 \le x \le M$

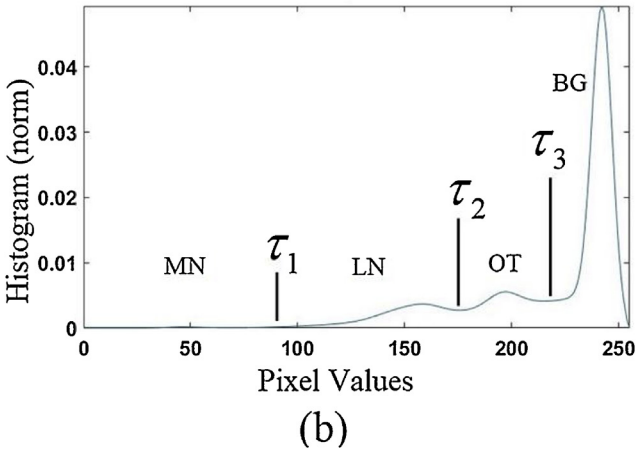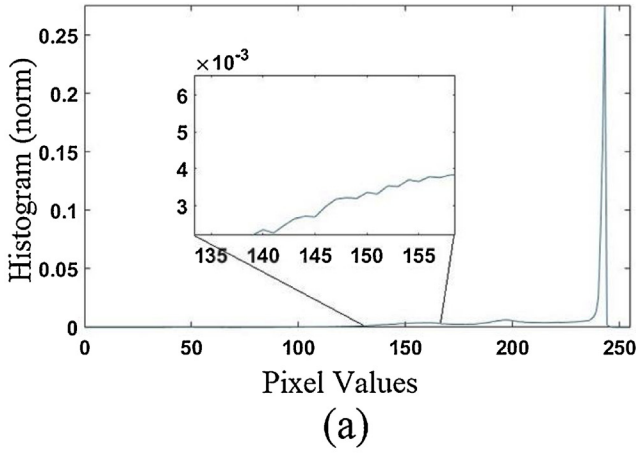**Fig. 2.** Schematic of the proposed segmentation technique.

Fig. 3. Histogram smoothing. a) original image histogram (normalized). b) smoothed histogram. MN: Melanoma, LN: Lymph node, OT: other tissue and BG: Background.
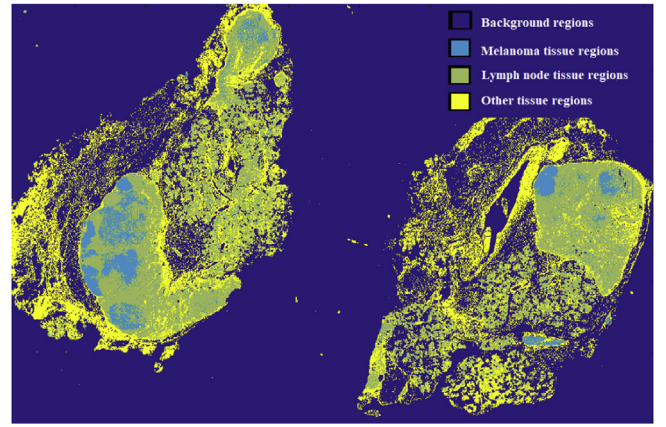

Fig. 4. Coarse pixel classification using thresholding. Light blue, yellow, green and dark blue pixels represent *Class 1, Class 2, Class 3* and *Class 4,* respectively.
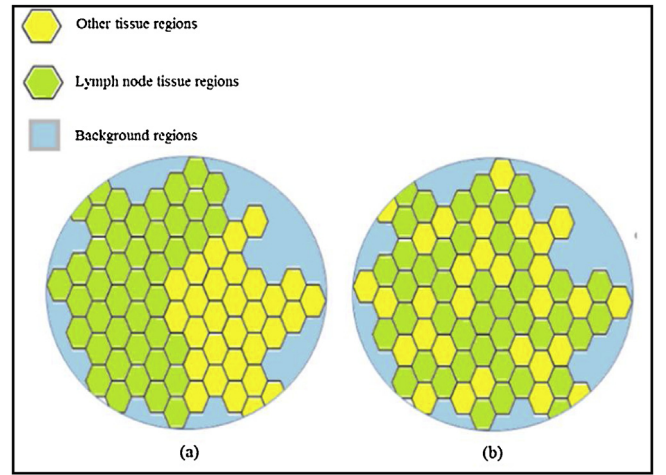

Fig. 5. Examples of neighbourhood $G_{x,y}$ in a classified image. a) neighbourhood with concentrated LN nuclei, b) neighbourhood with scattered LN neclei.

(rows), $1 \leq y \leq N$ (columns) using thresholding into four classes as follows:

$$\varphi(x, y) = \begin{cases} Class\ 1 & if \quad 0 \leq I(x, y) < \tau_1 \\ Class\ 2 & if \quad \tau_1 \leq I(x, y) < \tau_2 \\ Class\ 3 & if \quad \tau_2 \leq I(x, y) \leq \tau_3 \\ Class\ 4 & if \quad \tau_3 \leq I(x, y) \leq 255 \end{cases} \quad (1)$$

Note that the pixel values of these four classes, typically vary between [0-100], [70-160], [120-200], and [190-255]. Fig. 3 (b) shows the smoothed histogram corresponding to the image shown in Fig. 1, with $\tau_1 = 80$, $\tau_2 = 168$ and $\tau_3 = 203$. Fig. 4 shows the coarse classified φ obtained after thresholding.

3.2. Features extraction

In this module, the features are extracted from the coarse classified image φ, which will be used for fine segmentation in section C. A circular neighbourhood $G_{x,y}$ with radius r is defined for each classified pixel at coordinate (x, y). The neighbourhood $G_{x,y}$ includes $2\pi r^2$ pixels. Let the number of pixels belonging to *Class 1, Class 2, Class 3* and *Class 4* within the neighbourhood $G_{x,y}$ be denoted by ν_1, ν_2, ν_3 and ν_4, respectively. The normalized frequency count vector ν corresponding to the pixel at (x, y) is defined as follows:

$$\nu(x, y) = \begin{bmatrix} \nu_{1,n}, & \nu_{2,n}, & \nu_{3,n}, & \nu_{4,n} \end{bmatrix} \quad (2)$$

where $\nu_{i,n} = \dfrac{\nu_i}{2\pi r^2}$, $i = 1, ..., 4$.

Note that the feature vector ν does not represent the spreading pattern in the neighborhood $G_{x,y}$.

In Fig. 5 (a), the *Class 2* pixels are clustered together, and hence is more likely to be a lymph node tissue compared to Fig. 5 (b), where the *Class 2* pixels are scattered. Therefore, we consider using a High Frequency Measure (HFM) for $G_{x,y}$ and use it as a feature to distinguish the degree of scattering. The proposed frequency feature is also important to detect the other tissue regions, which are filled with holes and few parts of lymph node tissue. The following steps are used to calculate the HFM for each coarse classified pixel at coordinate (x, y):

1. Consider the pixel (x,y) as the origin of its neighborhood $G_{x,y}$. For simplicity we denote $G_{x,y}$ as G.
2. Unfold the G matrix by converting it from polar coordinates into Cartesian coordinates by arranging p radial lines (of length $2r + 1$) of G matrix which passes through the origin with angle $m\pi/p$, $0 \leq m \leq p-1$.
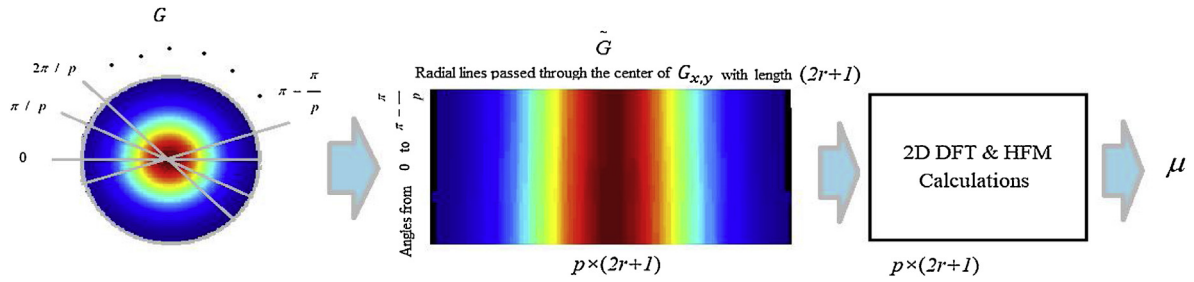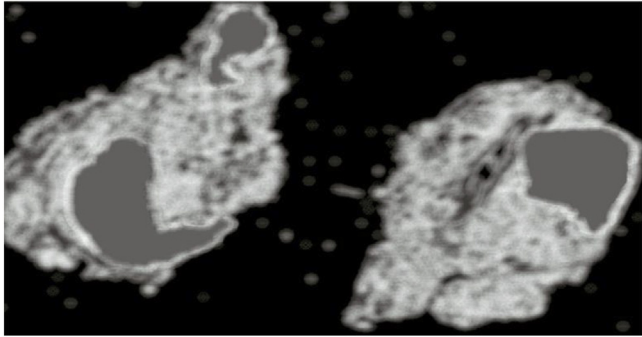
Fig. 6. Schematic to calculate the HFM.

Fig. 7. The HFM μ for the classified image φ shown in Fig. 4.

Arrange these radial lines as 2-D rectangular matrix $\tilde{G}$ of size $p \times (2r+1)$, as follows:

$$\tilde{G} = \begin{bmatrix} \tilde{G}(1,1) & \cdots & \tilde{G}(1, 2r+1) \\ \vdots & \ddots & \vdots \\ \tilde{G}(p,1) & \cdots & \tilde{G}(p, 2r+1) \end{bmatrix}$$

3 Calculate the 2-D- Discrete Fourier Transform (DFT) of $\tilde{G}$.

$$G'(q,k) = \sum_{m=1}^{p}\sum_{n=1}^{2r+1} \tilde{G}(m,n)\, e^{\frac{-j2\pi q(m-1)}{p}}\, e^{\frac{-j2\pi k(n-1)}{2r+1}} \tag{3}$$

$$1 \le q < p, \ 1 \le k < 2r+1$$

4 Calculate the HFM μ as follows:

$$\mu(x,y) = \sum_{q=\frac{p}{4}}^{\frac{3p}{4}} \sum_{k=\frac{r+1}{2}}^{\frac{3(2r+1)}{4}} \left|\left| G'(q,k) \right|\right| \tag{4}$$

where $\left|\left| G' \right|\right|$ is the magnitude of G', and the indices $[\frac{p}{4} : \frac{3p}{4}, \frac{r+1}{2} : \frac{3(2r+1)}{4}]$ are considered to represent the high frequency coefficients. Repeat steps 1–4 for all pixels in the image φ and calculate μ. Fig. 6 shows the overall schematic of the μ calculation. Fig. 7 shows the HFM μ corresponding to the image φ shown in Fig. 4. The HFM shows three contrast regions: black, gray and white, representing background, lymph nodes regions and other tissue regions, respectively.

The HFM μ is not directly used in the proposed method. Instead, a threshold is applied on μ to generate a binary HFM image μ^b as follows:

$$\mu^b(x,y) = \begin{cases} 0 \ \text{if } \mu(x,y) \le \tau_{Otsu} \\ 1 \ \text{if } \mu(x,y) > \tau_{Otsu} \end{cases} \tag{5}$$

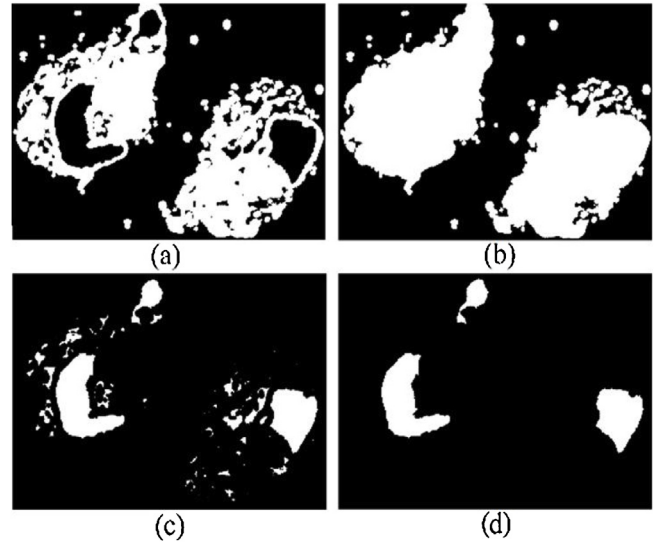where τ_{Otsu} is the Otsu threshold calculated from the pdf of μ.

Fig. 8. Images obtained by applying morphological operations on the image shown in Fig.4. (a) μ^b obtained using Otsu threshold, (b) μ_ℓ^{hf} obtained after filling the holes, (c) Initial estimate of lymph node H and (d) estimated lymph node area.

Fig. 8 (a) shows the binary HFM μ^b obtained by thresholding the image shown in Fig. 7. Note that the white pixels correspond to the other tissue (OT) regions whereas the black pixels denote the LN as well as the background. It would be helpful to distinguish the LN from the background region. The binary HFM also includes many small noisy (white) regions. Therefore, we propose to generate another binary HFM feature which will coarse segment the HFM image into LN and non-LN regions. This is obtained using the following steps.

(i) Note that the LNs appear as holes in the white background (consisting of OT regions). In the first step, we estimate the entire hole regions (i.e., all dark pixels surrounded by white pixels) in the image. In order to do this, the holes in μ^b are filled by dilation using the following iterative equation.

$$\mu_k^{hf} = (\mu_{k-1}^{hf} \oplus S_1) \cap (\sim \mu^b) \ k = 1, 2, 3, 4, \ldots \tag{6}$$

where the initial hole-filled image $\mu_0^{hf} = \mu^b$. Note that μ_k^{hf} is the hole-filled image after k-th iteration. The initial dilation with the structuring element S_1 starts inside the black holes, and the iteration is terminated when $\mu_k^{hf} = \mu_{k-1}^{hf}$ at $k = \ell$ (the last iteration). In this paper, we have used the following structuring element. Fig. 8 (b) is an example of the hole-filled image.

$$S_1 = \begin{bmatrix} 0 & 1 & 0 \\ 1 & 1 & 1 \\ 0 & 1 & 0 \end{bmatrix}$$
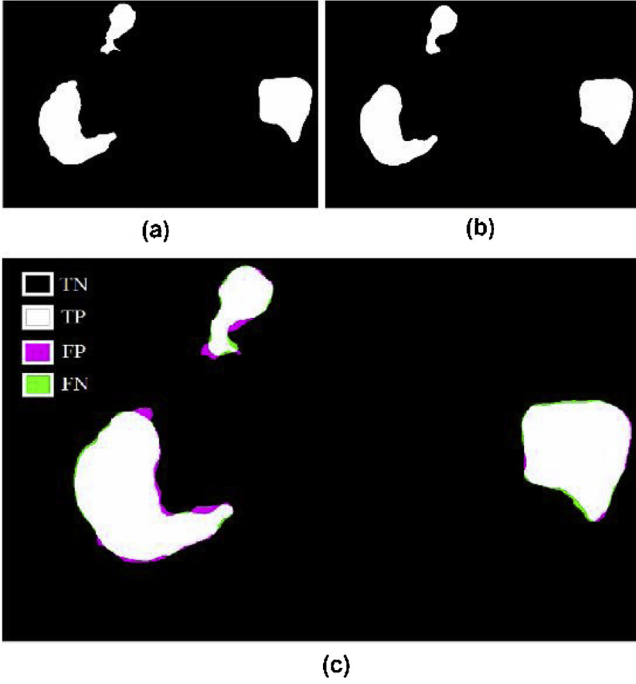
Fig. 9. Masks generated from the image in Fig.4. (a) Ground truth mask (b) Mask generated by the proposed technique and (c) comparison of ground truth and segmented mask.

- The hole regions filled up by Eq. (6) is calculated as:

$$H = \mu_\ell^{hf} - \mu^b \tag{7}$$

Note that the hole filling might fill some background regions. Fig. 8 (c) shows H obtained from Fig. 8 (b).

- It is observed that H contains many noisy areas. An 8-connectivity analysis is applied on H to determine the number and the size of the disconnected regions. We remove the regions with small areas that satisfies the following criterion:

$$area(R) < \tau_{area} * A_m \tag{8}$$

where R is a disconnected region, A_m is the largest size of the disconnected areas in H, and τ_{area} is a predetermined area thresholds parameter. The set of disconnected regions satisfying Eq. (8) is our initial estimate of the LN obtained from the HFM. Let these disconnected regions be denoted by L, and the number of regions be denoted by N_L.

The final feature vector for each pixel (x, y) in the input image I, is obtained by combining the three features as follows:

$$f = \{v(x, y), \mu^b(x, y), L(x, y)\} \tag{9}$$

where v represents the frequency count, μ^b is the binary HFM value and $L(x, y) = 1$ if the pixel is inside the L region, otherwise it is zero.

3.3. Fine segmentation

In this section, the feature vector f (with dimension 6) for each pixel in the image φ is classified (into LN and non-LN classes) using a Support Vector Machine (SVM). Let us assume that there are k training feature vectors $\{f_1, f_2, \cdots, f_k\}$ corresponding to k pixels which are randomly selected from the training images. The SVM model is trained using these selected k feature vectors and the corresponding labels $\{y_1, y_2, \cdots, y_k\}$. Note that, theses labels are obtained from the ground truth information where each feature
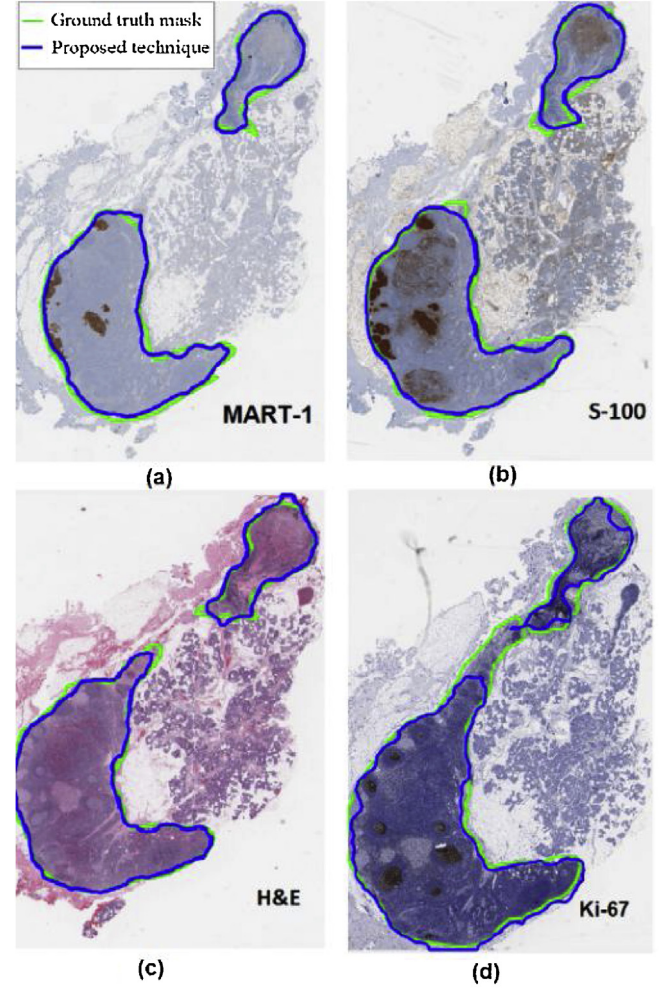

Fig. 10. Lymph nodes with different stains (a) MART-1, (b) S-100, (c) H&E (d) Ki-67.

vector is labelled as (1) for lymph node tissue or (-1) for non-lymph node tissue. The SVM estimates the best hyperplane P to separate these labelled feature vectors. The hyperplane P is defined by $w^T u + b = 0$, where u is a point on the hyperplane P. During training, optimal values of w and b are obtained by minimizing a cost function (Ben-Hur et al., 2001; Bishop, 2006). Note that an SVM classifier can also handle un-separable data by increasing the dimensionality with different kernels. During testing, the SVM model is used to generate the LN mask δ as follows:

$$\delta(x, y) = \{ \frac{1 \, for \, LN_{tissue}}{0 \, for \, non-LN_{tissue}}$$

3.4. Segmentation performance

The proposed technique is evaluated with 39 WSI images described in Section 2. Three WSIs (one MART-1, one Ki-67 and one H&E) are used as the training images to train the SVM model. The remaining 36 WSIs are used as the testing set for segmentation performance evaluation. Various parameter values used to evaluate the proposed technique are shown in Table 1. The following objective measures are used to compare the performance:

$$Sensitivity = \frac{TP}{TP + FN} \times 100\%$$

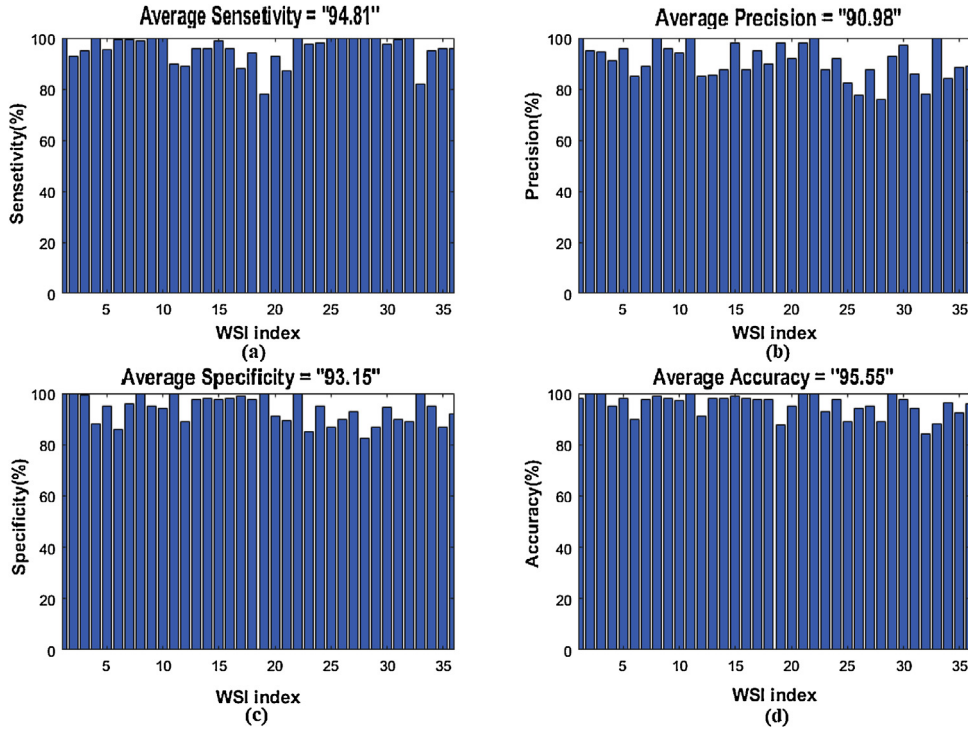$$Precision = \frac{TP}{TP + FP} \times 100\%$$

Fig. 11. Segmentation performance of the proposed technique for different image (a) Sensitivity, (b) Precision, (c) Specificity (d) Accuracy.

Table 1
Lymph Node Segmentation Parameters.

Down sampling factor	8
Neighborhood radius r	10 pixels
No. of radial lines, p	10
Area threshold (Eq. 8), τ_{area}	600 pixels

Table 2
Performance of the proposed technique using different SVM kernels.

Kernels	Sensitivity	Precision	Specificity	Accuracy
Linear	90.67	84.53	91.61	93.25
polynomial	89.34	88.22	93.03	93.89
Gaussian	94.81	90.98	93.15	95.55

$$Specificity = \frac{TN}{TN + FP} \times 100\%$$

$$Accuracy = \frac{TP + TN}{TP + FP + FN + TN} \times 100\%$$

where *TP*, *TN*, *FN* and *FP* denote the number of true positives, true negatives, false negatives and false positives, respectively.

Table 2 shows the performance comparison for three SVM kernels: linear, polynomial, and Gaussian. It is observed that the Gaussian kernel provides the best performance in terms of sensitivity, precision, specificity and accuracy. Therefore, all the subsequent results are obtained using the Gaussian kernel. Fig. 9 compares the segmented LN mask ϕ obtained by the proposed technique and the ground truth mask. Fig. 9(c) shows the obtained segmentation results overlapped with ground truth. Overall, it is observed that the LNs obtained by the proposed technique are very close to that of the ground truth. There is a thin layer of false positives around the LN contour, which is primarily caused due to the low values of HFM μ and high values of $v_{1,n}$, $v_{2,n}$ in these regions.

Fig. 10 shows examples of segmented Lymph nodes slides with different stains along with their ground truth masks. It is observed the segmented lymph nodes obtained by proposed technique are very close to the ground truth mask. Fig. 11 shows the sensitivity, precision, specificity and accuracy for each of the 36 images in the testing dataset. It is observed that the proposed technique provides an average sensitivity, precision, specificity, and accuracy of 94.55%, 90.98%, 93.15% and 95.55%, respectively. In other words, the LN segmentation performance is very good for most images. There are a few images where the sensitivity is somewhat low. For example, Fig. 10 shows that the WSI with indices 21, 24 and 33 have sensitivity around (80%). Visual inspection reveals that the low sensitivity for these images mainly arises because of the WSI artifacts such as tissue folding, slide imperfections, lighting inconsistencies, and improper calibration of imaging equipment.

4. Proliferation index calculation

In this paper, the Proliferation Index (*PI*) is calculated as follows:

$$PI = \frac{NA}{NP + NA} \times 100\% \tag{10}$$

where *NA* and *NP* are the number of the active and passive nuclei, respectively. In this paper, the following three types of PI values are calculated:

(i) The average PI value for the entire melanoma region.
(ii) The average PI value for each individual region.
(iii) The PI values for a given number (e.g., 3) of windows with size around (0.15×0.1) mm^2.

For PI calculation in a Ki-67 stained image of lymph node, MART-1 stained image is used to detect the melanoma regions which appear with brown color. Fig. 12 shows the schematic to calculate the *PI* values for the melanoma regions. It is observed that, there are four modules for *PI* calculations, which are detailed below.
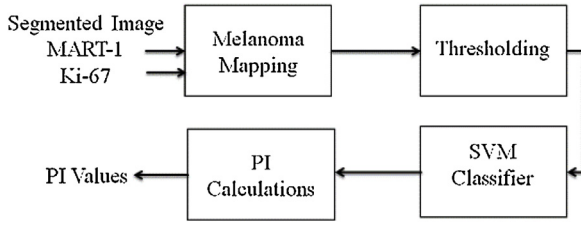
Fig. 12. Schematic of the proliferation index PI calculation.

4.1. Melanoma mapping

This module takes the segmented LN images corresponding to MART-1 and Ki-67 stained images (obtained using the technique proposed in section 3) as inputs. The melanoma regions of MART-1 stained image are mapped into affine transformed Ki-67 stained image using the following two steps.

Step-1 Ki-67 Transformation: Let the MART-1 and Ki-67 stained images be denoted by I_M and I_K, respectively. Let the binary LN masks of I_M and I_K be denoted by ϕ_M and ϕ_K, respectively. Fig. 10(a) shows a MART-1 image I_M and its LN mask ϕ_M (blue contour). On the other hand, Fig. 10 (d) shows Ki-67 image I_M and its LN mask ϕ_K (blue contour). In this step, we first register the LN masks ϕ_M and ϕ_K where the mask ϕ_M is kept fixed and the mask ϕ_K is transformed. The registration is achieved by finding the best transformation t' that will align the lymph node masks ϕ_M with ϕ_K in the same coordinate system. The transformation t' is obtained by solving the following equation.

$$t' = arg \max_{t} \lambda(\phi_M(X), \phi_K(t(X))) \qquad (11)$$

where $\lambda(.)$ is the mutual information and $t(x)$ is the affine transformation of the coordinate x. The mutual information of the two masks ϕ_M and ϕ_K is calculated as follows

$$\lambda(\phi_M, \phi_K) = e(\phi_M) + e(\phi_K) - e(\phi_M, \phi_K) \qquad (12)$$

where $e(\phi_M)$ and $e(\phi_K)$ are the entropies of mask ϕ_M and ϕ_K, respectively, and $e(\phi_M, \phi_K)$ is the joint entropy.

The entropies are calculated based on the probability density function (PDF) of the pixel values [0,1] of the entire 2D images ϕ_M and ϕ_K, and the joint entropy is calculated based on the joint PDF of ϕ_M and ϕ_K. Fig. 13 (a) shows the overlapped masks of ϕ_M (white and purple regions) and $\phi_K(t'(X))$ (white and green regions). After obtaining the optimal t', the affine transformation $t'(X)$ is applied on I_K as follows.

$$I'_K = I_K(t'(X)) \qquad (13)$$

where I'_K is the affine transformed Ki-67 stained image (see Fig. 13 (b)). The lymph nodes regions in I'_K masked by ϕ_M is calculated below:

$$I''_K = I'_K . * \phi_M \qquad (14)$$

where I''_K is LN regions in the affine transformed Ki-67 stained image I'_K as shown in Fig. 13 (c). Note that I''_K corresponds to the LNs of Ki-67 image that is also registered with the corresponding MART-1 image.

Step-2 Melanoma Mask: In order to calculate the PI, we also need a mask for the melanoma regions. In this work, the melanoma region mask δ is generated (for MART-1 only) as follows:

$$\delta(x, y) = \begin{cases} 1 & for \quad MNtissue \\ 0 & for \quad non-MNtissue \end{cases} \qquad (15)$$

where δ is the *Class 1* pixels obtained from coarse segmentation model (see Eq. (1)). Fig. 14 (a) shows the MN regions δ (with green
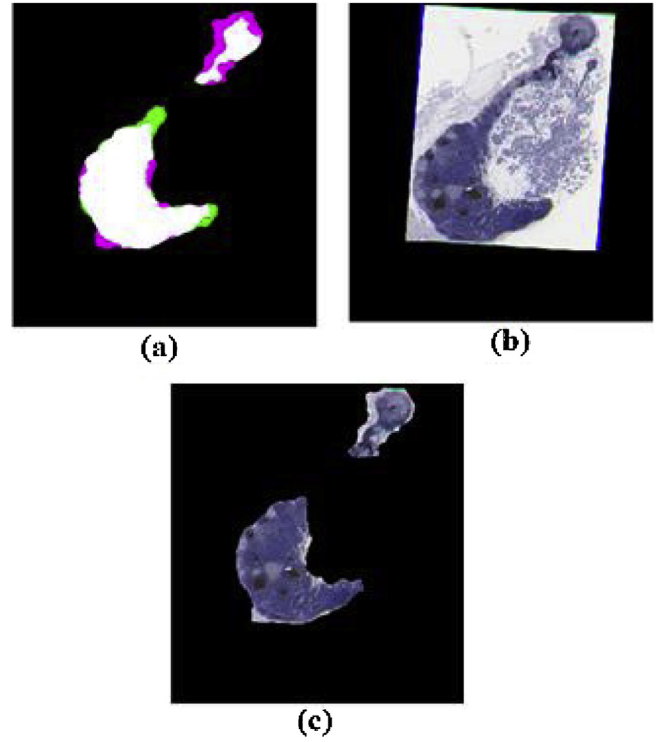

Fig. 13. Image registration for MART-1 and Ki-67 stained images for the same lymph nodes. (a) overlapped masks ϕ_M and ϕ_K after registration, (b) image I'_K, and (c) image I''_K.
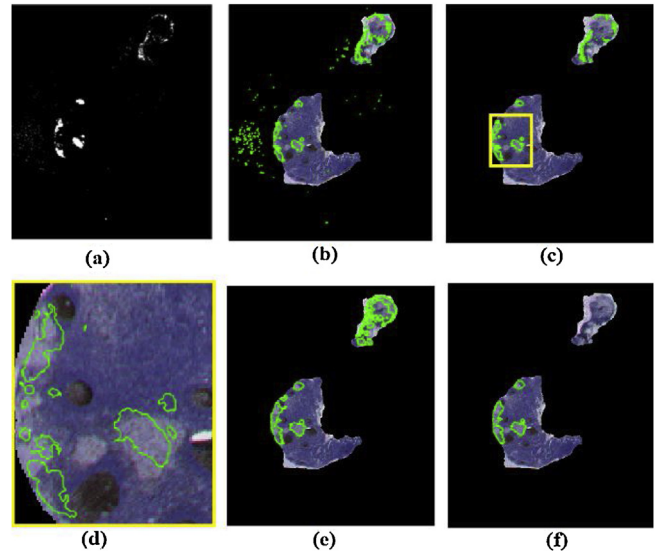

Fig. 14. Melanoma mapping process (a) Melanoma mask δ of MART-1, (b) δ contour melanoma regions (green color) in I''_K image, (c) δ' contour melanoma regions (green color) in I''_K image, (d) The magnified image of yellow square in δ', (e) δ'' contour melanoma regions (green color) in I''_K image and (f) The final melanoma mask.

contour) obtained for MART-1 image I_M. Fig. 14 (b) shows the mask δ superimposed on I''_K.

It is observed that some noisy melanoma areas (false detections) are outside the lymph nodes. These outside noisy areas are removed using the LN mask ϕ_M, and the de-noised mask is shown in Fig. 14(c). A magnified version of the yellow square in Fig. 14(c) is shown in Fig.14(d). It is observed that there are small disconnected MN regions inside the LN regions. The following steps are applied to connect these small regions and refine the MN mask δ:

1 An Active Contour Model (ACM) is applied on the melanoma contour to merge the small disconnected regions and make the melanoma mask smoother. The refinement of melanoma contour is driven by two forces: an internal force that keeps the contour smooth, and an external force that pushes it towards the object contour. The active contour model based on a gradient vector flow (Xu and Prince, 1998) is used in the proposed system for melanoma contour refinement. The melanoma contour, denoted by x(s), is obtained by minimizing E as defined below:

$$E = \int_0^1 [E_{\text{int}}(\mathbf{x}(s)) + E_{ext}(\mathbf{x}(s))]\, ds \qquad (16)$$

where, $\mathbf{x}(s) = [x(s), y(s)]$, $s \in (0, 1)$. The internal energy E_{int} is calculated as follows:

$$E_{\text{int}}(\mathbf{x}(s)) = \frac{1}{2}[\alpha |\mathbf{x}'(s)|^2 + \beta |\mathbf{x}''(s)|^2] \qquad (17)$$

where $\mathbf{x}'(s)$ and $\mathbf{x}''(s)$ are the first and second derivatives of $\mathbf{x}(s)$, respectively, and α and β are weighting parameters. The external energy E_{ext} of the contour is calculated as follows:

$$E_{ext} = \int \int [\gamma(u_x^2 + u_y^2 + v_x^2 + v_y^2) + |\nabla f| |k - \nabla f|^2]\, dxdy \qquad (18)$$

where $k = (u(x, y), v(x, y))$ is the gradient vector flow, f is the gradient of the smoothed image I''_K as the edge map, $\{u_x, u_y, v_x, v_y\}$ are the partial derivatives with respect to x and y. Fig. 14 (e) shows the melanoma regions after applying the ACM. Let the obtained melanoma mask be denoted by δ', and the disconnected region in δ' be denoted by R_i ($i = 1, 2, .., N_{DR}$) where N_{DR} is the number of disconnected candidate melanoma regions. It is observed in Fig. 14 (c) that there is a large number of R_i (in this example, N_{DR} =116).

2 The mask δ' is a smooth version of the mask δ, but there are a few regions of melanoma that expand on lymph melanoma regions due to the ACM. In this step, δ' is refined by removing regions that are not melanoma. This is done as follows: Convert the color image I_M into a gray intensity image I_{gM}. Map δ' onto I_{gM}, and calculate the mean intensity of each of the N_{DR} melanoma regions in I_{gM}. Note that the melanoma regions are typically brown and have a low mean intensity. Hence, a region R_i is removed from δ' if the corresponding mean intensity satisfies the following.

$$Mean\, Intensity(R_i) > \tau \qquad (19)$$

where τ is a threshold. Let the final melanoma mask be denoted by δ'', and let the number of remaining disconnected regions be denoted by N'_{DR}. It is observed in Fig. 14 (f) that there are three final melanoma regions (i.e., $N'_{DR} = 3$). The magnified version of these regions is shown in Fig. 15 (a).

4.2. Thresholding

Fig. 15 (a) shows the melanoma regions in I''_K, denoted by $\Re_i$ ($i = 1, 2, .., N'_{DR}$). We now want to segment the pixels in these regions into two classes: nuclei (*Class-1*) and background (*Class-2*). In this module, Otsu thresholding is used to perform the segmentation. A pixel located at (x,y) in region $\Re_i$ is classified as follows:

$$\Re_i^n(x, y) = \begin{cases} \Re_i(x, y) & if \quad gray(\Re_i(x, y)) \le \lambda_i \\ 0 & if \quad gray(\Re_i(x, y)) > \lambda_i \end{cases} \qquad (20)$$

where $\Re_i^n$ is the nuclei image, $gray(\Re_i(x, y))$ is the gray intensity of the color pixel $\Re_i(x, y)$, and λ_i is the Otsu threshold for $gray(\Re_i)$.

Note that in Eq. (20), the background pixels with gray value greater than λ_i in $\Re_i^n$ has been set to zero. Fig. 15 (b) shows the
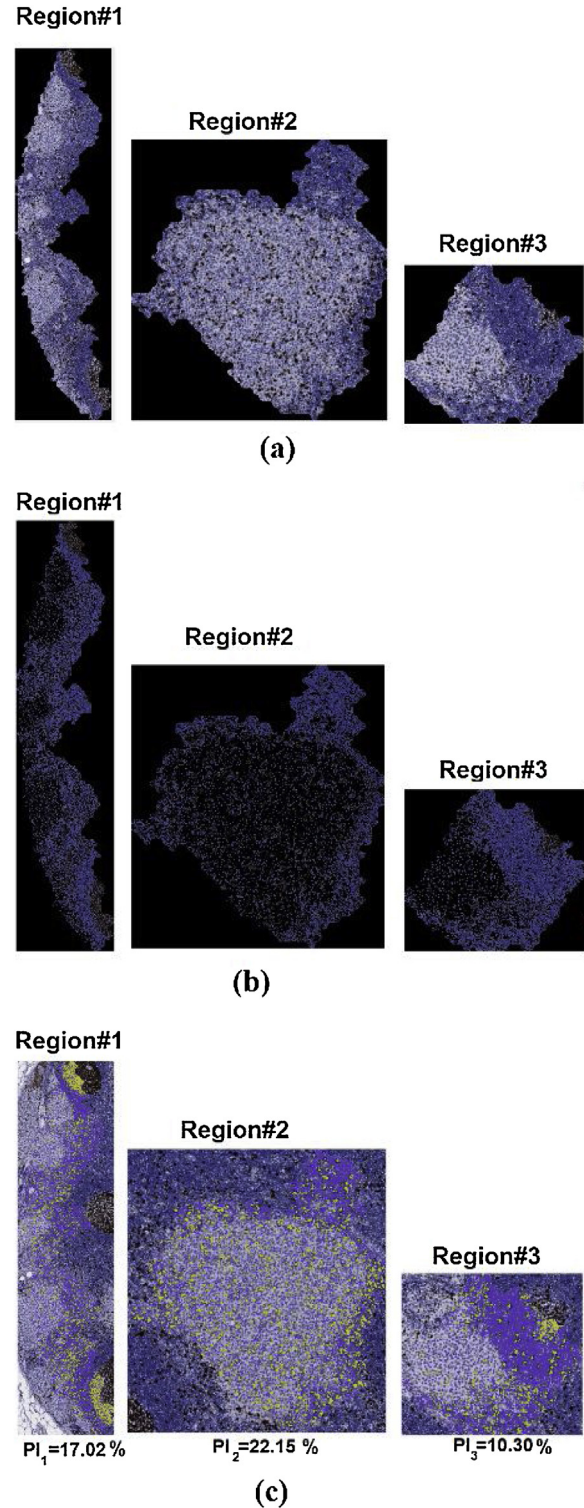

Fig. 15. Active and passive nuclei detection. (a) The melanoma regions in Ki-67 image (obtained from Fig.14(f)), (b) Nuclei mask using Otsu thresholding, (c) classified nuclei in Ki-67 image.

nuclei image for melanoma regions, where the *background* appears in black (i.e., zero intensity).

4.3. SVM classifier

In this module, an SVM model with linear kernel is trained to segment the nuclei regions $\Re_i^n$ into active nuclei (dark brown pixels)

and passive nuclei (blue pixels). The RGB values of a pixel are used as features, and the ground truth classification labels (i.e., active or passive) are manually obtained for each color pixel in $\Re_i^n$. The SVM model is trained using feature vector and classified label of pixels in the training images. The SVM model estimates the best hyperplane that separates the nuclei into active and passive nuclei. Let the SVM hyperplane parameters be denoted by w and b. The classification of a nuclei pixel (j) is done as follows.

$$pixel(j) = \begin{cases} Active & if & \left(w^T f_j + b\right) > 0 \\ Passive & if & \left(w^T f_j + b\right) \le 0 \end{cases} \quad (21)$$

where f_j is the feature vector corresponding to pixel j.

Fig. 15(c) shows an example of SVM classification results, where the active and passive nuclei are shown in yellow and purple colors, respectively. The SVM model presents a good performance for nuclei classification due to the strong difference between the brown and blue colors in RGB representation.

4.4. Proliferations index calculation

In current practice, pathologists typically calculate the PI values in a few small windows where there is a high concentration of active nuclei. This is primarily because of the difficulty of PI calculation using manual method. In this work, as the PI is calculated automatically, the following three types of *PI* values are calculated to give more information to the pathologists:

(i) One PI for each individual melanoma region $\Re_i$. Let the *PI* value of region $\Re_i$ be denoted by PI_i.
(ii) The average *PI* value for the entire melanoma region of a lymph node. Let this *PI* be denoted by PI_E.
(iii) The PI values for a few windows with largest concentration of active nuclei. If K windows are selected, let the *PI* be denoted by $PI_{W,k}, k = 1, 2, ..., K$.

We first calculate the PI_i values for all individual melanoma regions $\Re_i$ using Eq. (10). Fig. 15 (c) shows the PI_i value for each of the three individual melanoma regions.

For the entire melanoma region, the PI_E value is calculated as follows:

$$PI_E = \frac{NA_{all}}{NP_{all} + NA_{all}} \times 100\% \quad (22)$$

where NA_{all} and NP_{all} are the numbers of the active and passive nuclei, respectively, in the entire melanoma regions. For the lymph node in Fig. 15 (c), the PI_E value is obtained as 19.82%.

The $PI_{W,k}, k = 1, 2, ..., K$, values are calculated for the dense active nuclei window automatically as follows:

(i) Consider an active nucleus located at (x, y). Calculate the PI value of the window (size: $m \times n$), centred at (x, y). Let the PI value be denoted by $\rho_{x,y}$.
(ii) Calculate $\rho_{x,y}$ for each active nucleus in the melanoma region. The highest K values of $\rho_{x,y}$ are then selected, and are denoted by $PI_{W,k}, k = 1, 2, ..., K$ (typically $K = 3$) with $PI_{W,1}$ being the highest value.

Fig. 16 shows three windows in red contour with high PI values: $PI_{W,1} = 22.59\%, PI_{W,2} = 19.98\%, PI_{W,3} = 24.83\%$.

4.5. Performance evaluation

In this section, we evaluate the performance of the nuclei segmentation and PI calculation with parameters shown in Table 3.
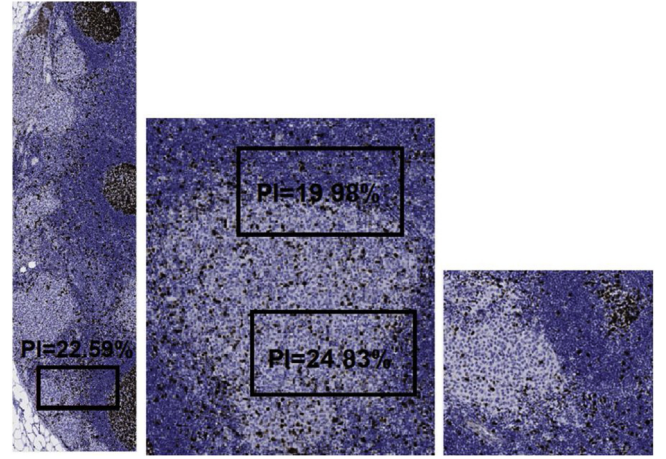

Fig. 16. The PI values for three windows (in black contour) for melanoma regions. The third image does not have a region with high PI value. Note that each of the three windows is of size around $0.15 \times 0.1 \ mm^2$.

Table 3
PI calculation Parameters.

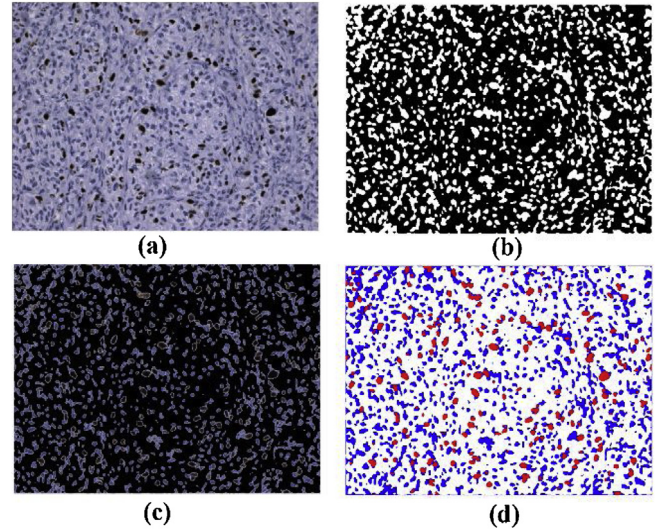|	
Window size	$0.15 \times 0.1 \ mm^2$
τ (the normalized melanoma threshold in δ')	0.5
K (number of the windows)	3

Fig. 17. The proposed nuclei segmentation (a) The Ki-67 stained image (b) Otsu mask, (c) the nuclei mask and (d) the segmentation results using SVM, where the active and passive nuclei are shown in red and blue, respectively.

To evaluate the PI calculation performance, we generate 14 subimages (each with 1920×2500 pixels) from 9 Ki-67 WSIs, which are manually labelled by doctors. Two of these 14 subimages are used to train the SVM (for classifying the nuclei pixels into passive and active pixels). The remaining 12 subimages are used as the testing dataset for the performance evaluation.

Fig. 17(a) shows a selected window of a Ki-67 image of a lymph node. The thresholded image is shown in Fig. 17(b) where the white pixels represent nuclei and black pixels represent the background. The nuclei pixels (both active and passive), obtained using Eq. 21, are shown in Fig. 17(c). The classified nuclei, obtained using the SVM model, are shown in Fig. 17(d), where the active
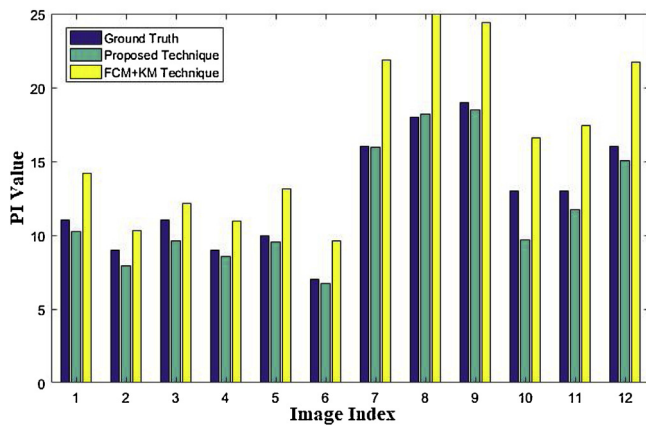
Fig. 18. Performance comparison of the proposed technique (in green bars) and the FCM + KM (Mungle and Tewary, 2017) technique (in yellow bars). The Ground Truth is shown in blue bars.

Table 4
PI calculation performance of proposed, and FCM + KM techniques.

Technique	RMSE	MAE	Execution time (in s)
FCM + KM (Mungle and Tewary, 2017)	4.20	3.76	298.20
Proposed PI	1.25	0.89	15.74

and passive nuclei are represented by red, and blue color (the background pixels are shown in green). It is observed that the active and passive nuclei are efficiently classified to obtain the PI values.

The performance of the proposed technique is compared with the FCM + KM technique proposed by Mungle et al. (Mungle and Tewary, 2017). The FCM and K-means functions available in the MATLAB toolbox, with two clusters, were used to evaluate the FCM + KM technique. For FCM, a threshold of 0.5 was used for the nuclei segmentation. After K-means clustering, all active nuclei candidates with an area less than 600 pixels (physical area: 0.125 μm^2) were considered as noisy areas and not used for PI calculation. The PI calculation is performed using a window size of 1920×2500 pixels (physical dimension: $0.238 \times 0.310 mm^2$) on a Ki-67 image scanned with 20X magnification. Fig. 18 shows the PI values of 12 image windows, obtained by using the FCM + KM and the proposed techniques, along with the ground truth PI values. Table 4 compares the Root Mean Square Error (RMSE), Mean absolute Error (MAE) of the obtained PI values (compared to the ground truth). It is observed that the proposed technique provides a superior performance compared to the FCM + KM technique. A possible reason for the superior performance is that the proposed technique uses supervised SVM classifier whereas the FCM + KM technique uses the unsupervised K-means method, which may not be very effective.

Table 4 also compares the execution time (on a Windows 10 computer with Intel i7-4790 CPU and 12 GB RAM with MATLAB R2018a) for the proposed technique and the FCM + KM technique. It is observed that the proposed *PI* technique is about 20 times faster compared to the FCM + KM technique.

5. Conclusion

This paper proposes a fully automated technique for lymph node segmentation and proliferative index calculation in lymph node histopathological images. The technique uses local frequency features and SVM classifier for lymph node segmentation in biopsy images stained with H&E, Ki-67, Mart-1, S-100, and CD-45. The technique then identifies the melanoma region in Ki-67 image based on the Mart-1 image characteristics of the same lymph node. Thresholding and SVM classification are then used to determine active and passive nuclei. The technique then calculates PI value of the entire melanoma region, individual melanoma region as well as for a few windows with high concentration of active nuclei. Experimental results show that the technique provides an excellent performance in terms of both lymph node segmentation and PI calculation.

References

Alturkistani, H., Tashkandi, F., Mohammed, Z., 2016. Histological stains: a literature review and case study. Glob. J. Health Sci. 8 (3), 72–79.

American Cancer Society, [Online]. Available: 2018. Cancer Facts and Figures. https://www.cancer.org/content/dam/cancer-org/research/cancer-facts-and-statistics/annual-cancer-facts-and-figures/2018/cancer-facts-and-figures-2018.pdf.

Balch, C., Gershenwald, J., Atkins, M., Buzaid, A., Cascinelli, N., Cochran, A., et al., 2010. Melanoma of the skin. In: Edge, S., Byrd, D., Compton, C., Fritz, A., Greene, F., Trotti, A. (Eds.), AJCC Cancer Staging Manual. , 7th ed. Springer, New York, pp. 325–344.

Bánkfalvi, A., 2000. Comparative methodological analysis of erbB-2/HER-2 gene dosage, chromosomal copy number and protein overexpression in breast carcinoma tissues for diagnostic use. Histopathology 37 (November 5), 411–419.

Ben-Hur, A., Horn, D., Siegelmann, H., Vapnik, V., 2001. Support vector clustering. J. Mach. Learn. Res. 2, 125–137.

Bishop, C., Appendix E 2006. Pattern recognition and machine learning. In: Kung, S.Y., Mak, M.W., Lin, S.H. (Eds.), Biometric Authentication: A Machine Learning Approach. Springer, Prentice Hall, 2005, Chapter 4.

Bruno, S., Darzynkiewicz, Z., 1992. Cell cycle dependent expression and stability of the nuclear protein detected by Ki-67 antibody in HL-60 cells. Cell Prolif. 25 (January 1), 31–40.

Giuliano, A., Kirgan, D., Guenther, J., et al., 1994. Lymphatic mapping and sentinel lymphadenectomy for breast cancer. Ann. Surg. 220 (September 3), 391–401.

Hanahan, D., Weinberg, R., 2011. Hallmarks of cancer: the next generation. Cell 144 (5), 646–674.

International Agency for Research on Cancer, 2014. World Cancer Report 2014. World Health Organization, Geneva, Switzerland, pp. 146–147, Chapter 2.8.

Ismail, S., Colclough, A., Dinnen, J., Eakins, D., Evans, D., Gradwell, E., et al., 1989. Observer variation in histopathological diagnosis and grading of cervical intraepithelial neoplasia. BMJ: Br. Med. J. 298 (March 6675), 707–710.

Kothari, S., Phan, J., Wang, M., 2013. Eliminating tissue-fold artifacts in histopathological whole-slide images for improved image-based prediction of cancer grade. J. Pathol. Inform. 4.22.

Mungle, T., Tewary, S., et al., 2017. Automated characterization and counting of Ki-67 protein for breast cancer prognosis: a quantitative immunohistochemistry approach. Comput. Methods Prog. Biomed. 139, 149–161.

Nawaz, K., Khaja, M., Nazriya, R., 2016. Reliability of sentinel lymph node biopsy in head and neck squamous cell carcinoma. Int. J. Otorhinolaryngol. Head Neck Surg. 2 (2), 105–109.

Petushi, S., Garcia, F., Haber, M., Katsinis, C., Tozeren, A., 2006. Large-scale computations on histology images reveal grade-differentiating parameters for breast cancer. BMC Med. Imaging 6 (14), 1–11.

Siegel, R.L., Miller, K.D., Jemal, A., 2019. Cancer statistics, 2019. CA Cancer J. Clin. 69 (January/February 1), 7–34.

Steger, S., Ebert, D., Erdt, M., 2011. Lymph node segmentation in CT slices using dynamic programming. 2011 IEEE International Symposium on Biomedical Imaging: From Nano to Macro, 1990–1993.

Wang, Y., Crookes, D., Eldin, O., Wang, S., Hamilton, P., Diamond, J., 2009. Assisted diagnosis of cervical intraepithelial neoplasia (cin). IEEE J. Select. Top. Signal. Process. 3 (1), 112–121.

Wu, H., Phan, J., Bhatia, A., Shehata, B., Wang, M., 2015. Detection of blur artifacts in histopathological whole-slide images of endomyocardial biopsies. Proc. 37th Annual International Conference of the IEEE Engineering in Medicine and Biology Society, 727–730.

Xu, H., Mandal, M., 2015. Epidermis segmentation in skin histopathological images based on thickness measurement and k-means algorithm. EURASIP J. Image Video Process. 2015 (1), 1–14.

Xu, C., Prince, J., 1998. Snakes, shapes, and gradient vector flow. IEEE Trans. Image Process. 7 (3), 359–369.

Xu, H., Berendt, R., Jha, N., Mandal, M., 2017. Automatic measurement of melanoma depth of invasion in skin histopathological images. Micron 97, 56–67.

Zhang, Y., Ying, M.T.C., Yang, L., Ahuja, A.T., Chen, D.Z., 2016. Coarse-to-fine stacked fully convolutional nets for lymph node segmentation in ultrasound images. 2016 IEEE International Conference on Bioinformatics and Biomedicine (BIBM), 443–448.

Salah Alheejawi received his B-Tech degree in Communication engineering from the Middle Euphrates Technical University, Iraq, in 2009, and M-Tech degree in Communication & Information System from Aligarh Muslim University, India, in 2013. He has been working towards the pH.D. degree in Electrical Engineering in the Multimedia Computing and Communication Lab, Department of Electrical Engineering, University of Alberta, Edmonton, AB, Canada, since 2015. His research interests include medical image analysis, pattern recognition, and computer vision. Mr. Alheejawi is recipient of a scholarship from MOHESR, Iraq for his pH.D. studies.

Hongming Xu received the B.Sc. and M.Sc. degrees in Computer Engineering from the Information Engineering College, Northwest A&F University, Shaanxi, China, in 2009 and 2012, respectively and the pH.D. degree in Electrical and Computer Engineering from the University of Alberta, Edmonton, AB, Canada, in 2017. He is currently working sssas a postdoctoral fellow in the Cleveland Clinic, USA. His main research interests include medical image analysis, machine learning and deep learning related biomedical applications. His current project is to apply machine learning and deep learning methods to do cancer grading and gene mutation prediction.

Richard Berendt attended medical school at the University of Alberta, Edmonton, AB, Canada. He then joined the Laboratory Medicine and Pathology residency program at the Cross Cancer Institute, University of Alberta. Dr. Berendt is certified in both Clinical Pathology and Anatomic Pathology and General Pathology and Anatomical Pathology in Canada.

Naresh Jha received the Bachelor of Medicine and Bachelor of Surgery degrees from Delhi University, New Delhi, India, in 1979. He became a Fellow of the Royal College of Physicians of Canada in radiation oncology in 1987. Since 1988, he has been a Senior Radiation Oncologist at the Cross Cancer Institute, University of Alberta, Edmonton, AB, Canada. He specializes in head and neck, thyroid, and skin cancers. He is also a pioneer of the submandibular salivary gland transfer which is a ground breaking technique to prevent radiation-induced xerostomia.

Mrinal Mandal received the B.E. degree in Electronics and Communication Engineering from the National Institute of Technology, Durgapur, India, in 1987, the M.E. degree in Electronics and Communication Engineering from the Indian Institute of Engineering Science and Technology, India in 1989, and the M.A.Sc. and pH.D. degrees in Electrical and Computer Engineering from the University of Ottawa, Canada, in 1995 and 1998, respectively. He is currently a Full Professor in the Department of Electrical and Computer Engineering, University of Alberta, Edmonton, AB, Canada. He has authored the book Multimedia Signals and Systems (Springer) and coauthored the book Continuous and Discrete Time Signals and Systems (Cambridge Univ. Press). His current research interests include medical image analysis, image and video processing, and. He has published more than 180 papers in refereed journals and conferences, and has a U.S. patent on lifting wavelet transform architecture. He has been the Principal Investigator of projects funded by Canadian Networks of Centers of Excellence such as CITR and MICRONET and is currently the Principal Investigator of a project funded by the NSERC. Prof. Mandal is a past recipient of Canadian Commonwealth Fellowship and Humboldt Research Fellowship (Germany).